Biaxial fluid oscillations can propel a microcapsule swimmer in an arbitrary direction

doi: 10.1103/PhysRevE.98.063102

Biaxial fluid oscillations can propel a microcapsule swimmer in an arbitrary direction

Takeru Morita,[1] Toshihiro Omori,[1] and Takuji Ishikawa[1,2,*]

[1]*Department of Finemechanics, Graduate School of Engineering, Tohoku University, 6-6-01 Aoba, Aramaki, Aoba-ku, Sendai 980-8579, Japan*

[2]*Graduate School of Biomedical Engineering, Tohoku University, 6-6-01 Aoba, Aramaki, Aoba-ku, Sendai 980-8579, Japan*

(Received 11 September 2018; published 7 December 2018)

Due to their potential usefulness in engineering and medical applications, various artificial microswimmers have been proposed. In our previous paper *et al.* [T. Morita, T. Omori, and T. Ishikawa, Phys. Rev. E **98**, 023108 (2018)], we introduced a microcapsule swimmer that underwent amoeboidlike shape deformation under vertical fluid oscillation and showed the advantages of using a solid membrane and fluid oscillation in terms of swimmer controllability. Although the microcapsule was capable of migrating in the Stokes flow regime, the propulsion direction was limited to vertically upward or downward. In this paper, therefore, we attempted to control the propulsion of a microcapsule in an arbitrary direction by imposing biaxial fluid oscillations, which is a major step toward future applications. Numerical results showed that the microcapsule could migrate in the horizontal and vertical directions by imposing biaxial fluid oscillations in the vertical and horizontal planes, respectively. The horizontal propulsion can be understood in terms of effective and recovery strokes, i.e., a stroke swimmer, whereas vertical propulsion is similar to rigid body motion induced by a torque, i.e., a torque swimmer. By sequentially imposing three types of fluid oscillations, we successfully controlled the microswimmer to draw a Π-shaped trajectory. Thus, these results illustrate that the position and trajectory of the microswimmer can be controlled arbitrarily in three dimensions. The knowledge presented in this paper is important for future artificial microswimmer designs.

DOI: 10.1103/PhysRevE.98.063102

I. INTRODUCTION

Due to their potential usefulness in engineering and medical applications, various types of artificial microswimmers have been proposed [1,2] that utilize magnetic forces [3–6], electric forces [7–9], chemical forces [10–14], optical forces [15,16], or phoretic forces [17–19] for propulsion. Although swimming motion is strongly influenced by the hydrodynamics of the surrounding fluid, previous studies have rarely utilized the hydrodynamic forces generated by fluid oscillations, with the exception of a few studies [20–22]. In this paper, fluid oscillations were used to propel a microswimmer; the advantages of this approach are that the oscillations are easily generated via system vibrations and that the oscillation strength does not decay rapidly with distance.

The flow field around a microswimmer may be regarded as Stokes flow, due to the swimmer's small size. In the Stokes flow regime, simple reciprocal body deformation cannot generate net migration; this is known as the Scallop theorem [23,24]. To overcome the Scallop theorem, several groups have proposed amoeboidlike nonreciprocal body deformation for net propulsion [25]. Because the degree of freedom in the deformation is much larger in a continuum than in a system consisting of a few rigid body segments, amoeboidlike body deformation can be an effective strategy for swimming. Avron *et al.* [26] reported optimal deformation of a two-dimensional swimming amoeboid. Misbah and colleagues investigated three-dimensional amoeboid swimming in an unbounded fluid [27] and in confined geometries [28,29], in which the membrane was assumed to be a two-dimensional incompressible fluid. Recently, Nasouri *et al.* proposed a swimmer consisting of two linked spheres, wherein one sphere is rigid and the other is an incompressible neo-Hookean solid [30]. Although these previous papers form the fundamental basis for amoeboid swimming in Stokes flow, our understanding has to be strengthened much further to design an actual amoeboid microswimmer.

In our previous paper [31], we proposed a microcapsule swimmer with a solid membrane that could create amoeboidlike body deformation by imposing vertical fluid oscillations. The solid membrane has several advantages over a fluid membrane: (1) coalescence of the membranes can be prevented, (2) the reference shape can be controlled, and (3) the motion can be deterministically predicted. The proposed microswimmer consisted of an elastic capsule containing fluid and a rigid sphere. The densities of the internal fluid and sphere were different; thus, opposing forces were generated when fluid oscillations were applied. These forces induced nonreciprocal body deformation of the microswimmer, by which it could migrate in Stokes flow. The direction of propulsion, however, was limited to vertically upward or downward, depending on the capsule's aspect ratio. Thus, the microswimmer's position and the trajectory could not be controlled in three dimensions.

In this paper, therefore, we attempted to control the propulsion of the microcapsule in an arbitrary direction for future applications. Although the microcapsule used was the same as that used in our previous paper [31], it exhibited *rich* phenomena by imposing biaxial fluid oscillations instead of uniaxial oscillations, i.e., fluid oscillations generated in a plane. We

*Corresponding author: ishikawa@bfsl.mech.tohoku.ac.jp

numerically showed that the fluid oscillations induced dramatic change in the propulsion of a microcapsule swimmer, and the propulsion could be controlled in an arbitrary direction.

The paper is organized as follows. In Sec. II, we explain the basic equations and numerical methods used to represent the motion of the microswimmer. In Sec. III, we investigate horizontal locomotion created by imposing biaxial fluid oscillations in the vertical plane. In Sec. IV, we examine vertical locomotion by imposing biaxial fluid oscillations in the horizontal plane. We describe controlled microcapsule propulsion via biaxial fluid oscillations to draw a Π-shaped trajectory in Sec. V. Concluding remarks are presented in Sec. VI.

II. BASIC EQUATIONS AND NUMERICAL METHODS

A. Problem settings

The problem settings are similar to those used in our previous paper [31]. Briefly, the microswimmer consists of an elastic membrane with a prolate spheroidal reference shape containing a rigid sphere. The rigid sphere is connected to the capsule membrane by linear springs, as shown in Fig. 1. The lengths of the major and minor axes of the reference shape are a_1 and a_2, respectively.

We assume that the densities of the surrounding fluid ρ_∞, the fluid inside the capsule ρ_c, and the rigid sphere ρ_r satisfy the inequality $\rho_c < \rho_\infty < \rho_r$, such that a large ratio of ρ_r to ρ_∞ can be achieved. A large ρ_r to ρ_∞ ratio is preferable, as the rigid sphere becomes sufficiently small to generate a large deformation of the capsule. The average density of the microswimmer ρ_0 is defined as follows:

$$\rho_0 = \frac{V_c\rho_c + V_r\rho_r}{V_c + V_r}, \tag{1}$$

where V_c is the volume of the fluid inside the capsule, V_r is the volume of the rigid sphere, and $V_c + V_r$ is the volume of the whole microswimmer. The value of ρ_0 is assumed to be almost the same as the surrounding fluid. Gravity acts in the negative z direction, as shown in Fig. 1. The viscosities of the surrounding fluid and the fluid inside the capsule are assumed to be identical for simplicity.

We assumed that an oscillating force acts on the entire system. The oscillating force may be generated by vibrating a tank containing the microswimmer or by a sound wave with a much larger wavelength than that of the microswimmer. The acceleration of the fluid oscillation $\underline{\alpha}$ is given by

$$\underline{\alpha} = (|\underline{g}|A_x \sin(2\pi f t + \phi_x), |\underline{g}|A_y \sin(2\pi f t + \phi_y), |\underline{g}|A_z \sin(2\pi f t + \phi_z)), \tag{2}$$

where $\underline{g}$ is the gravitational acceleration, A_i is the amplitude in the i direction, f is the frequency, t is time, and ϕ_i is the phase in the i direction. Due to the fluid oscillation, opposing forces are induced between the fluid inside the capsule and the rigid sphere. The oscillation forces deform the capsule, which, in turn, induces microswimmer propulsion.

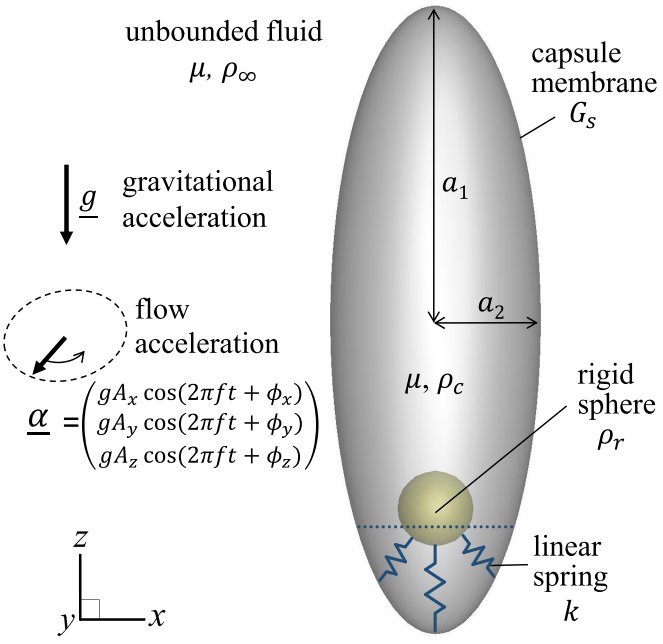

FIG. 1. Basic structure of the microswimmer and the problem settings. Acceleration vector $\underline{\alpha}$ of the fluid oscillations is given as a function of time. The gravitational acceleration $\underline{g}$ is imposed in the $-z$ direction. The dotted line on the capsule indicates the area under which spring forces are considered.

B. Governing equations

The governing equations are similar to those used in our previous papers [31–33]. For the capsule, we solved the solid mechanics of the membrane and the fluid mechanics of the internal and external fluids. For the rigid sphere, the fluid mechanics were solved based on the force and torque conditions.

1. Fluid mechanics for the capsule

Due to the microswimmer's small size, we neglect inertial effects and assume Stokes flow. In the Stokes flow regime, the velocity at the capsule membrane can be expressed by a boundary integral equation, as follows [34]:

$$\underline{u} = -\frac{1}{8\pi\mu}\int \underline{\underline{J}}\,\underline{q_c} dS_c - \frac{1}{8\pi\mu}\int \underline{\underline{J}}(\rho_c - \rho_\infty)\{(\underline{g} + \underline{\alpha})\cdot\underline{r}\} \times \underline{n} dS_c - \frac{1}{8\pi\mu}\int \underline{\underline{J}}\,\underline{q_r} dS_r - \frac{1}{8\pi\mu}\int \underline{\underline{J}}\,\underline{q_{sp}} dS_c' \tag{3}$$

where the number of bars under each variable indicates the tensor rank, $\underline{u}$ is the velocity, μ is the viscosity, $\underline{q_c}$ is the traction jump across the membrane, $\underline{r}$ is the position vector, $\underline{q_r}$ is the traction force on the rigid sphere surface, and $\underline{q_{sp}}$ is the force density induced by the linear springs. S_c, S_c', and S_r are the surfaces of the whole capsule membrane, that of the membrane connected by springs, and that of a rigid sphere, respectively. The second-order tensor $\underline{\underline{J}}$ is the Green's function for an unbounded fluid, and $\underline{n}$ is the outward normal vector with respect to the capsule surface. The first term on the right-hand side of Eq. (3) indicates the capsule deformation contribution; the second term indicates the contributions of gravity and fluid oscillations; the third term represents the

contribution of the rigid sphere; and the fourth term corresponds to the contribution of the springs.

2. Solid mechanics of the capsule membrane

We assume that the thickness of the capsule membrane is much smaller than the capsule size and has a typical radius of curvature. Thus, we consider only the deformation in the median surface, in which the membrane is modeled as a two-dimensional hyperelastic material.

By considering both the in-plane stretch and bending rigidity of the membrane, the traction jump across the membrane $\underline{q_c}$ in Eq. (3) may be expressed as $\underline{q_c} = \underline{q_s} + \underline{q_b}$, where $\underline{q_s}$ is the force density due to the in-plane stretch and $\underline{q_b}$ is the force density due to the bending rigidity. The Skalak model [35] is employed as a constitutive law of in-plane tension, and the Helfrich model [36] is applied for bending rigidity. By neglecting the inertia effect on the membrane motion, the equilibrium equation between $\underline{q_s}$ and the in-plane tension $\underline{\underline{\sigma}}$ can be represented in the weak form as [37]

$$\int \underline{v} \cdot \underline{q_s}\, dS_c = \int \underline{\underline{\epsilon}} : \underline{\underline{\sigma}}\, dS_c, \tag{4}$$

where $\underline{v}$ and $\underline{\underline{\epsilon}}$ are the virtual displacement and strain, respectively.

3. Fluid mechanics for the rigid sphere

On the surface of the rigid sphere, the velocity is described by Eq. (3). To satisfy the rigid body motion and no-slip boundary conditions, the velocity on the surface of the rigid sphere must satisfy the following:

$$\underline{u} = \underline{U_r} + \underline{x} \times \underline{\Omega_r}, \tag{5}$$

where $\underline{U_r}$ and $\underline{\Omega_r}$ are the translational and rotational velocities of the rigid sphere, respectively, and $\underline{x}$ is the position on the surface of the sphere.

The force condition of the rigid sphere is given by

$$\int \underline{q_r} dS_r = \int \frac{V_r(\rho_r - \rho_c)}{V_c} \{(\underline{g} + \underline{\alpha}) \cdot \underline{r}\} \underline{n} dS_c + \int \underline{q_{sp}} dS_c'. \tag{6}$$

The left-hand side indicates the hydrodynamic force. The first term on the right-hand side represents the force generated by gravity and fluid oscillations. The last term in Eq. (6) describes the spring force, which is integrated over the capsule surface connected by springs S_c'. We assume a linear spring with equilibrium length l_0, and the spring force density $\underline{q_{sp}}$ is given by

$$\underline{q_{sp}} = k(|\underline{s}| - a_r - l_0) \frac{\underline{s}}{|\underline{s}|}, \tag{7}$$

where $\underline{s}$ is a vector connecting a material point on the capsule membrane to the center of the rigid sphere, k is the spring strength, and a_r is the radius of the rigid sphere. The rigid sphere is connected by springs to the bottom of the membrane only, as opposed to the entire membrane. The ratio of S_c' to S_c was set as 15% in the initial reference shape, where S_c' is specified by the dotted line in Fig. 1. The spring force density $\underline{q_{sp}}$ does not generate any torque on the rigid sphere; thus, a torque-free condition was assigned in this case.

4. Nondimensionalization

The governing equations are nondimensionalized using characteristic length a_c, defined as $a_c = \sqrt[3]{a_1 a_2^2}$, characteristic velocity $|\rho_c - \rho_\infty| g {a_c}^2/\mu$, and membrane shear elastic modulus G_s that appears in the Skalak law [35]. In the main text, symbol * indicates dimensionless quantities.

C. Numerical methods

The numerical methods used here are similar to those used in our previous papers [31–33,38]. Briefly, the solid mechanics of the membrane were solved using the finite element method. A boundary element method was applied to solve the fluid mechanics. A second-order Runge-Kutta method was employed for time marching. The capsule membrane was divided into 5120 triangular elements with 2562 nodes, and the rigid sphere surface was divided into 320 triangular elements with 162 nodes.

D. Parameters

We used the same density and volumetric conditions as in our previous paper [31] to highlight the change in propulsion direction that occurs by modifying the fluid oscillation conditions. To generate a sufficiently strong force and to make the capsule deformation significant, we used the conditions $\rho_r/\rho_c = 20$ and $(V_c + V_r)/V_r = 4^3$. We also assumed that the microswimmer was almost neutrally buoyant and that opposing forces were generated on the rigid sphere and the fluid inside the capsule due to the fluid oscillation. The average density of the microswimmer was set as $\rho_0/\rho_\infty = 1.001$, as in our previous paper [31]. The parameters of the in-plane stretch (Bond number) and the bending rigidity remained fixed throughout this paper as $|\rho_c - \rho_\infty| g a_c^2/G_s = 1.0$ and $E_b/G_s a_c^2 = 0.1$, where E_b is the bending modulus of the Helfrich model [36]. The spring parameters remained fixed at $k a_c^2/G_s = 100$ and $l_0^* = 0.2$. The fluid oscillation frequency was held constant at $f^* = 2$. These values were used so that we could observe sufficiently large deformations of the capsule and to ensure that the in-plane tension played a major role in the capsule deformation.

In Sec. III, we impose biaxial fluid oscillations in a "vertical plane" to generate a horizontal migration. Three parameters were varied: the oscillation amplitude in the x direction A_x, the phase difference of the fluid oscillation between the x and z directions $\phi_x - \phi_z$, and the aspect ratio of the capsule a_1/a_2. Other parameters remained fixed at $A_y = 0$ and $A_z = 20$.

In Sec. IV, we consider biaxial fluid oscillations in a "horizontal plane" to generate vertical migration. We varied the aspect ratio of the capsule a_1/a_2, while keeping the other parameters as $A_x = A_y = 10$, $A_z = 0$, $\phi_x = 0$, and $\phi_y = -\pi/2$. These parameter sets were selected so as to show relevant phenomena and to explain the propulsion mechanisms.

In Sec. V, we describe a microswimmer with $a_1/a_2 = 3$, sequentially exposed to three kinds of fluid oscillations to achieve a Π-shaped trajectory. The details of the three oscillations—(1) uniaxial vertical fluid oscillation, (2) biaxial fluid oscillation in a vertical plane, and (3) biaxial fluid

oscillation in a horizontal plane—will be explained further in this section.

III. HORIZONTAL PROPULSION IN BIAXIAL FLUID OSCILLATIONS IN A VERTICAL PLANE

A. Horizontal propulsion of the microswimmer

We first show that the microswimmer can migrate in the horizontal direction by imposing biaxial fluid oscillations in the vertical plane. Locomotion of a microswimmer with $a_1/a_2 = 3$ is shown in Fig. 2 under the conditions of $A_x = 10$, $\phi_x = 0$, and $\phi_z = -\pi/2$ (see also movie 1 in Supplemental Material [39]). The acceleration vector of the fluid oscillation $\underline{\alpha}$ in this case drew an ellipse, as shown in Fig. 2(b). Due to the fluid oscillation, opposing forces are induced between the fluid inside the capsule and the rigid sphere. The capsule is stretched at $t/T = n$ and compressed at $t/T = n + 1/2$, where T is the period of oscillation. The capsule shapes differ at $t/T = n + 1/4$ and $n + 3/4$, such that the capsule undergoes nonreciprocal body deformation.

The time dependencies of the x and z components of $\underline{r_{cc}}^*$ are plotted in Fig. 2(c), where $\underline{r_{cc}}^* = (x^*_{cc}, y^*_{cc}, z^*_{cc})$ is the vol-

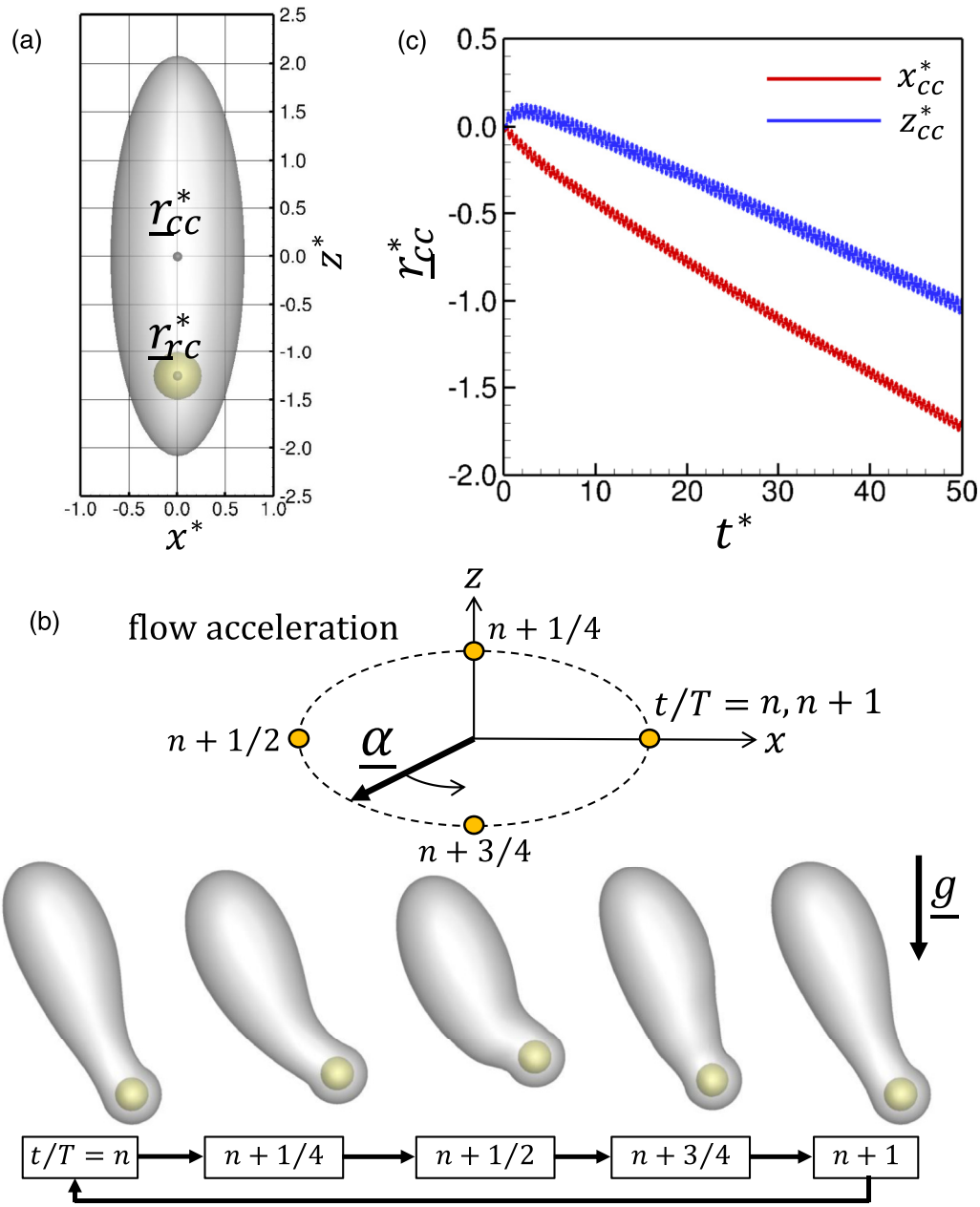

FIG. 2. Horizontal propulsion of the stroke swimmer ($a_1/a_2 = 3$, $A_x = 10$, $A_z = 20$, $A_y = 0$, $\phi_x = 0$, and $\phi_z = -\pi/2$). (a) Initial reference shape. The volumetric centers of the microswimmer and the rigid sphere are $\underline{r_{cc}}^*$ and $\underline{r_{rc}}^*$, respectively. (b) Periodic deformation of the capsule during one period of oscillation, where T is the period and n is an integer (see also movie 1 in Supplemental Material [39]). The upper graph shows the time dependence of flow acceleration during one oscillation period in the x and z directions. (c) Time dependence of the x and z components of $\underline{r_{cc}}^*$. Periodic motion is observed when $t^* \geqslant 5$.

umetric center of the microswimmer [see Fig. 2(a)]. x_{cc}^* and z_{cc}^* decreased over time, although they tended to fluctuate over the time scale of the fluid oscillation. The time change became periodic for $t^* \geqslant 5.0$; thus, capsule deformation may also become periodic within this time scale. Figure 2 clearly shows that the microswimmer is capable of migrating horizontally, as well as vertically, by imposing biaxial fluid oscillations in the vertical plane.

In our previous paper [31], the microswimmer undergoing uniaxial vertical fluid oscillation could migrate the distance of about $6 \times 10^{-3} a_c$ during one oscillation period. In Fig. 2(c), on the other hand, the microswimmer undergoing biaxial fluid oscillations migrated the distance of about $1.6 \times 10^{-2} a_c$ during one oscillation period, more than double that of the previous paper. Thus, migration via biaxial fluid oscillations can be more effective than that under vertical oscillation conditions.

B. Propulsion mechanism of the stroke swimmer

In this section, we investigate the propulsion mechanism of the microswimmer shown in Fig. 2. To discuss the nonreciprocal body deformation of the microswimmer, we plotted the trajectory of the rigid sphere center $\underline{r_{rc}}^*$ relative to the microswimmer center $\underline{r_{cc}}^*$, i.e., $\underline{r_{rc}}^* - \underline{r_{cc}}^*$, in Fig. 3(a). The length between $\underline{r_{rc}}^*$ and $\underline{r_{cc}}^*$ is $l^*(= |\underline{r_{rc}}^* - \underline{r_{cc}}^*|)$, and the microswimmer migrates in the negative x direction. We see that the rigid sphere moves in the positive x direction with a large value of l^*, whereas it moves in the negative x direction with a small value of l^*. Thus, the body deformation is clearly nonreciprocal and capable of inducing net migration under Stokes flow conditions.

As shown in Fig. 2(b), the microswimmer migrated in the negative x direction from $t^*/T = 0$ to about 0.49, such that the stroke in this time period may be regarded as an "effective" stroke. On the other hand, the microswimmer migrated in the positive x direction from $t^*/T \cong 0.49$ to 1; the stroke in this time period may be regarded as a "recovery" stroke. Due to the difference in thrusts between the effective and recovery strokes, the microswimmer migrates in the negative x direction. The swimming mechanism is similar to the effective and recovery strokes of swimming microorganisms [40]; thus, we refer to this swimmer as a "stroke swimmer".

To effectively discuss the propulsion efficiency, we propose a function $\underline{\lambda}^*$ defined by $\underline{\lambda}^* = (\lambda_x^*, \lambda_y^*, \lambda_z^*) = -(\underline{u_{rc}}^* - \underline{u_{cc}}^*)l^*$, where $\underline{u_{rc}}^*$ is the velocity of the rigid sphere and $\underline{u_{cc}}^*$ is the velocity of the volumetric center of the microswimmer. We note that its time-averaged value during the one period of oscillation $\underline{\lambda}_{\rm ave}^* = \int_T \underline{\lambda}^* dt$ can be nonzero, although that of the relative velocity $\int_T \underline{u_{rc}}^* - \underline{u_{cc}}^* dt$ is zero in the case of periodic motion. λ_x^* is negative during the effective stroke and positive during the recovery stroke, as shown in Fig. 3(b). The curve of λ_x^* looks like the time derivative of x_{cc}^*,; thus, $\underline{\lambda}^*$ appears to be analogous to the propulsion velocity generated by the stroke. The time-averaged value of λ_x^* is negative, which is the same direction as the net migration. This suggests that $\underline{\lambda}_{\rm ave}^*$ is a good measure of the propulsion efficiency, which will be discussed further in the next section.

There are three essential ingredients required to generate the net propulsion of the microswimmer: (1) the density mismatch between the rigid sphere and the fluid inside the capsule, (2) gravity or springs, and (3) the elasticity of the capsule membrane. Without the density mismatch, no external force is generated by the fluid oscillations and nothing happens. Even with the density mismatch, if there is no gravity or springs, the rigid sphere may eventually drift around the center of the capsule, and the capsule deformation becomes symmetric between the effective and recovery strokes. Such a reciprocal deformation cannot induce net migration in Stokes flow. Once gravity is introduced, as well as a density mismatch, the time-averaged position of the rigid sphere has a certain offset from the center of the capsule, which can break the symmetry. The asymmetry can be generated by either gravity or springs, i.e., both are not necessary. Here, we introduce both, because the gravitational field is unavoidable in our daily life and because the springs are efficient in localizing the rigid sphere in the vicinity of the capsule bottom, thus reducing

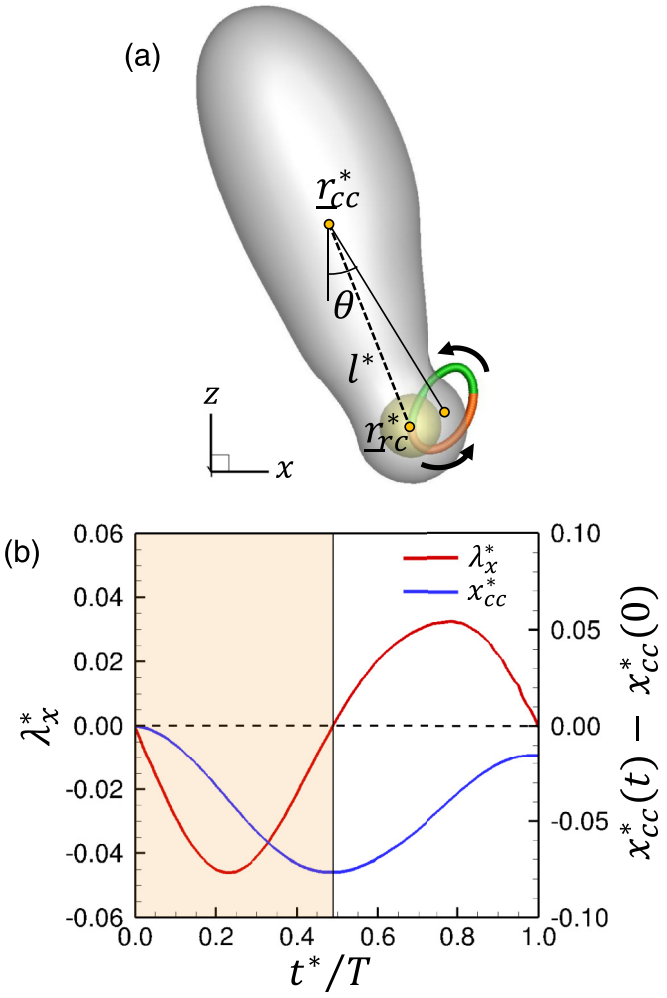

FIG. 3. Horizontal migration mechanism, where the orange color indicates the effective stroke and the green color indicates the recovery stroke ($a_1/a_2 = 3$, $A_x = 20$, $\phi_x = 0$, and $\phi_z = -\pi/2$). (a) Relative trajectory of $\underline{r_{rc}}^*$ from $\underline{r_{cc}}^*$ during one oscillation period, plotted for the capsule shape at $t/T = n$. θ is the angle between the $-z$ direction and the time-averaged vector of $\underline{r_{rc}}^* - \underline{r_{cc}}^*$. (b) Time dependence of λ_x^* and the x component of the volumetric center of the microswimmer x_{cc}^* during one oscillation period.

the computational time required to achieve periodic motion. The last ingredient is the elasticity of the capsule membrane. The microswimmer must be stretched during the effective stroke and compressed during the recovery stroke, so as to generate nonreciprocal body deformation. The capsule must have some deformability, given that a rigid ellipsoid containing a rigid sphere cannot migrate in fluid oscillations.

C. Parametric study of the stroke swimmer

1. Amplitude of the fluid oscillation in the x direction

In this subsection, we investigate the effect of fluid oscillation amplitude in the x direction A_x. We calculated the time-averaged velocities of the microswimmer in the range $2 \leqslant A_x \leqslant 14$, under the conditions of $A_z = 20$, $a_1/a_2 = 3$, and $\phi_x - \phi_z = \pi/2$, as shown in Fig. 4(a). The range of A_x was selected such that the time-averaged horizontal propulsion velocity $\overline{u_x^*}$ becomes sufficiently large compared with the vertical velocity $\overline{u_z^*}$. $\overline{u_x^*}$ and $\overline{u_z^*}$ decreased as A_x increased, and the microswimmer migrated in the negative x and z directions in the large A_x regime. In the range $2 \leqslant A_x \leqslant 10$, the swimmer migrated more horizontally than vertically.

We also plotted the x and z components of $\underline{\lambda}^*_{\mathrm{ave}}$, i.e., $\lambda^*_{\mathrm{ave},x}$ and $\lambda^*_{\mathrm{ave},z}$, as shown in Fig. 4(b). We see similar tendencies between Figs. 4(a) and 4(b). Thus, we can confirm that $\underline{\lambda}^*_{\mathrm{ave}}$ can be a good measure of the propulsion tendencies, and the propulsion mechanism can be understood by effective and recovery strokes.

2. Aspect ratio

Next, we investigated the effect of aspect ratio a_1/a_2 in the range $1.0 \leqslant a_1/a_2 \leqslant 4.0$, under the conditions of $A_x = 10$ and $\phi_x - \phi_z = \pi/2$, as shown in Fig. 4(c). The microswimmer with $a_1/a_2 \leqslant 2.5$ migrated more vertically than horizontally. In the case with $3 \leqslant a_1/a_2$, on the other hand, the microswimmer migrated more horizontally than vertically.

We also plotted $\lambda^*_{\mathrm{ave},x}$ and $\lambda^*_{\mathrm{ave},z}$ in Fig. 4(d). Although the ratio of $\lambda^*_{\mathrm{ave},x}$ to $\lambda^*_{\mathrm{ave},z}$ was not exactly the same as that of $\overline{u_x^*}$ to $\overline{u_z^*}$, the basic tendencies were captured by $\underline{\lambda}^*_{\mathrm{ave}}$. Thus, we again confirmed that $\underline{\lambda}^*_{\mathrm{ave}}$ can be a good measure of the propulsion tendencies.

3. Phase difference

Lastly, we examined the effect of phase difference $\phi_x - \phi_z$ in the range $0 \leqslant \phi_x - \phi_z \leqslant \pi$ under the conditions of $A_x = 10$ and $a_1/a_2 = 3$, as shown in Fig. 4(e). We note that the results with $\pi \leqslant \phi_x - \phi_z \leqslant 2\pi$ can be replicated from those with $0 \leqslant \phi_x - \phi_z \leqslant \pi$ due to the symmetry of the problem. In Fig. 4(e), the time-averaged horizontal velocity $\overline{u_x^*}$ showed the minimum value near $\phi_x - \phi_z = 0.75\pi$. When $\phi_x - \phi_z = 0.875\pi$, the absolute value of $\overline{u_z^*}$ had a minimum value and the ratio of $\overline{u_x^*}$ to $\overline{u_z^*}$ reached its maximum value. Thus, under these conditions, the microswimmer migrated mainly in the horizontal direction. When $\phi_x - \phi_z = 0$, $\overline{u_x^*}$ is positive while $\overline{u_z^*}$ is negative. These results illustrate that the direction of net migration can be controlled by changing the phase difference $\phi_x - \phi_z$, even without changing other parameters.

The effect of $\phi_x - \phi_z$ on the propulsion may be understood using the attitude angle θ between the $-z$ axis and the time-averaged vector of $\underline{r_{rc}}^* - \underline{r_{cc}}^*$, as defined in Fig. 3(a). The attitude angle shown in Fig. 4(e) has a positive peak at around $\phi_x - \phi_z = 0.375\pi$, while it was almost zero near $\phi_x - \phi_z = 0.8\pi$, as shown in Fig. 4(e). The attitude of the microswimmer with $\phi_x - \phi_z = 0.8\pi$ was almost vertical, thus providing a possible explanation for the horizontal migration of the microswimmer.

We also plotted $\lambda^*_{\mathrm{ave},x}$ and $\lambda^*_{\mathrm{ave},z}$, as shown in Fig. 4(f). Again, we see similar tendencies between $\overline{\underline{u^*}}$ and $\underline{\lambda}^*_{\mathrm{ave}}$. Thus, the propulsion mechanism can be explained by effective and recovery strokes, as well as the attitude of the microswimmer.

IV. VERTICAL PROPULSION IN BIAXIAL FLUID OSCILLATIONS IN A HORIZONTAL PLANE

Vertical propulsion was investigated in our previous paper [31], in which uniaxial vertical fluid oscillations were imposed. Here, we show that vertical propulsion can be achieved by biaxial fluid oscillations in the horizontal plane, and that the direction of locomotion can be opposite to that reported in our previous paper [31].

A. Vertical propulsion of the microswimmer

In Fig. 5(a), we show the deformation of the microswimmer with $a_1/a_2 = 3$ under biaxial fluid oscillation conditions in the horizontal plane (see movie 2 in Supplemental Material [39]). Given the conditions of $A_x = A_y = 10$, $\phi_x = 0$, and $\phi_y = -\pi/2$, the rotational acceleration field is generated in the horizontal plane, which causes the rigid sphere to rotate around the body axis, as shown in Fig. 5(a). The motion of the microswimmer may be regarded as being in a steady state in the reference frame rotating with the acceleration field, given that the microswimmer moves with a constant rotational velocity with the same shape. In other words, nonreciprocal body deformation cannot be observed in this case. Thus, the migration mechanism is expected to be different from that of the stroke swimmer.

The time dependence of $\underline{r_{cc}}^*$ is plotted in Fig. 5(b). We see that the x and y components of $\underline{r_{cc}}^*$ oscillated over time, due to the rotational fluid oscillation in the x-y plane. The z component, however, decreased steadily after $t^* \geqslant 5$, where the motion is considered to be in a steady state in the reference frame rotating with the acceleration field. The result clearly illustrates that the microswimmer can propel itself vertically downward, even though the fluid oscillations are imposed in the horizontal plane. We note that in our previous paper [31] the microswimmer with $a_1/a_2 = 3$ migrated vertically upward under uniaxial vertical fluid oscillation conditions. Hence, the direction of motion can be reversed by changing the fluid oscillations.

B. Propulsion mechanism of the torque swimmer

The microswimmer shape satisfies the steady state in the reference frame rotating with the acceleration field, as shown in Fig. 6(a). To understand the basic vertical propulsion mechanism, we simplified the problem and assumed that the microswimmer undergoes rigid body motion, although the capsule membrane actually has some slip velocity. In the Stokes flow regime, rigid body motion, in response to

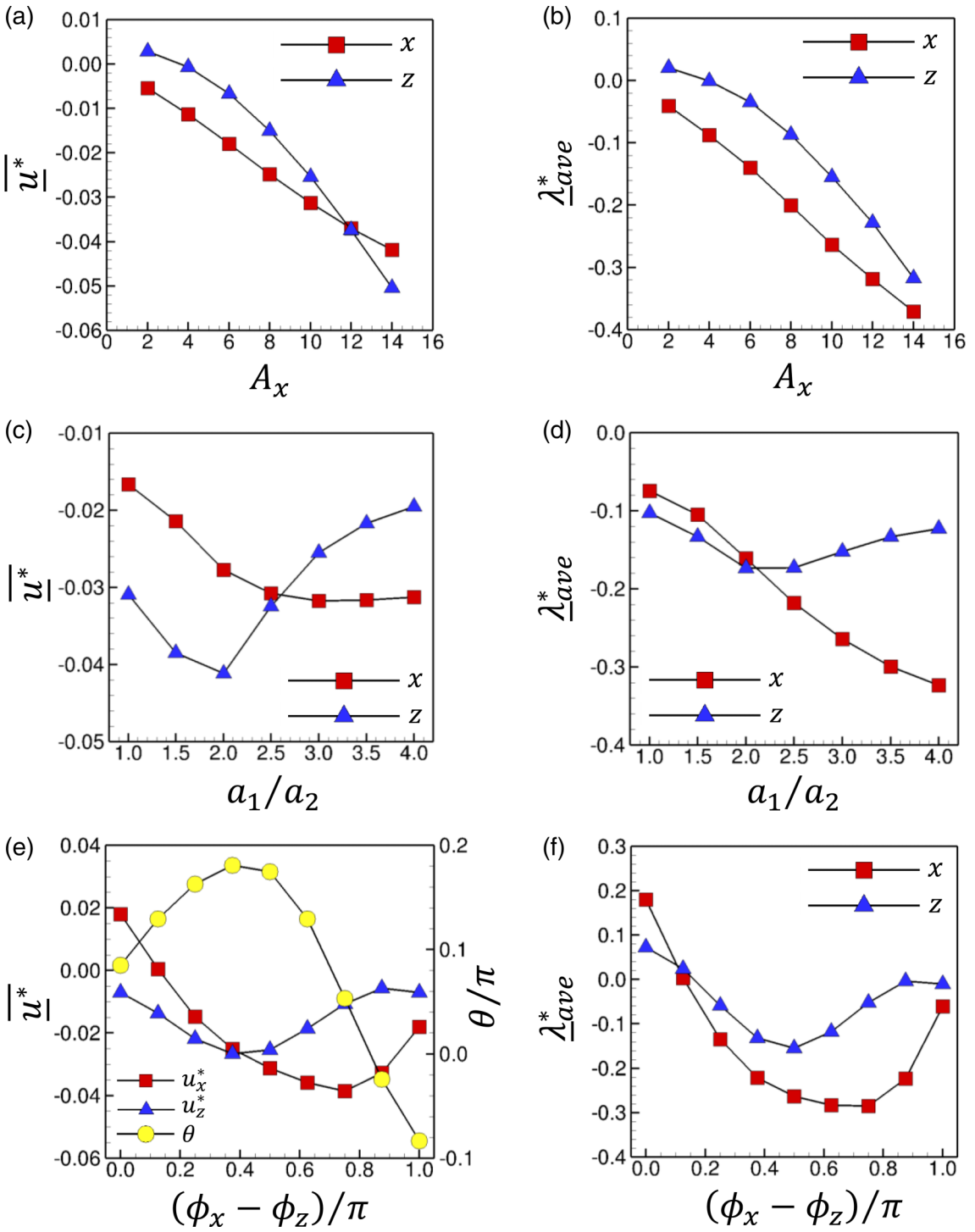

FIG. 4. Effect of parameters a_1/a_2, A_x, and $\phi_x - \phi_x$ on the time-averaged propulsion velocity $\overline{\underline{u}^*}$ (a, c, e) and the function $\underline{\lambda}^*_{\text{ave}}$ (b, d, f). The effects of (a, b) the amplitude of fluid oscillation A_x ($a_1/a_2 = 3$ and $\phi_x - \phi_z = \pi/2$), (c, d) the aspect ratio a_1/a_2 ($A_x = 10$ and $\phi_x - \phi_z = \pi/2$), and (e, f) the phase difference between $\phi_x - \phi_z$ ($A_x = 10$ and$a_1/a_2 = 3$). In (e), the attitude angle θ is also plotted.

the prescribed forces and torques, is classified as a mobility problem [41]. Here we solved the mobility problem of the microswimmer under the assumption of rigid body motion.

We first calculated the external torque exerted on the microswimmer. Due to the density mismatch, force $\underline{F}_c$ acts on the fluid inside the capsule, and $\underline{F}_r$ acts on the rigid sphere, as schematically shown in Fig. 6(b). Although the two external forces nearly cancel each other out, i.e., creating a force-free scenario, a net torque of $(\underline{F}_c - \underline{F}_r) \times (\underline{r}_{cc} - \underline{r}_{rc})/2$ remains. To simplify the discussions about torque, we define another coordinate system $\eta - \zeta - \xi$ in which the origin is located at

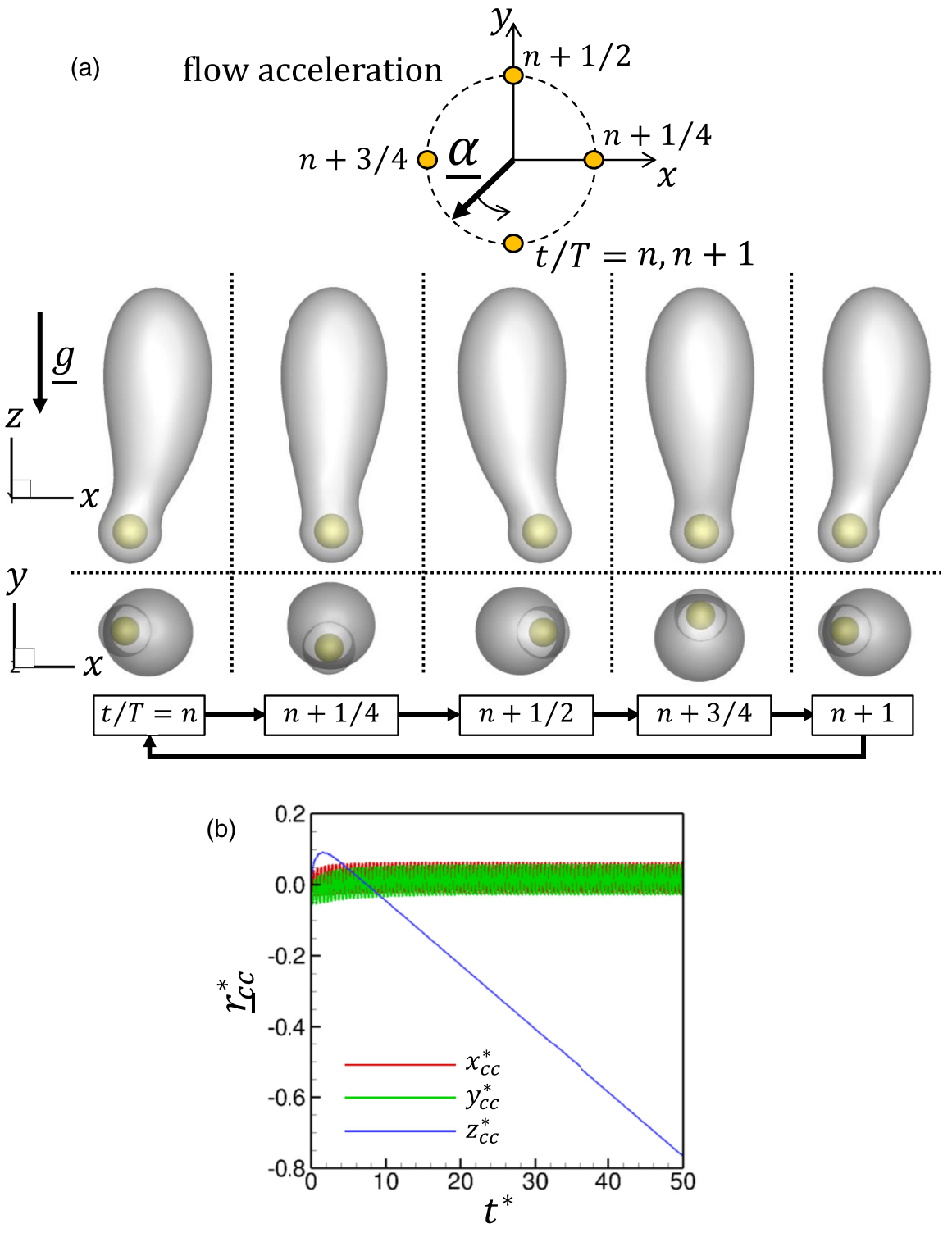

FIG. 5. Downward propulsion of the torque swimmer ($a_1/a_2 = 3$, $A_x = A_y = 10$, $A_z = 0$, $\phi_x = 0$, and $\phi_y = \pi/2$). (a) Periodic deformation of the capsule during one oscillation period, where T is the period and n is an integer (see also movie 2 in Supplemental Material [39]). The upper graph shows the time dependence of flow acceleration during one oscillation period in the x and y directions. (b) Time dependence of the x, y, and z components of $\underline{r_{cc}}^*$. Periodic motion is observed when $t^* \geqslant 5$.

$\underline{r_{rc}}^*$, as shown in Fig. 6(c). The η axis is taken in the direction of $\underline{r_{cc}}$ from $\underline{r_{rc}}$. The ξ axis is defined as $\underline{\xi} = \underline{\eta} \times \frac{(\underline{\eta} \times \underline{z})}{|\underline{\eta} \times \underline{z}|}$, where $\underline{z}$ is the unit vector of the z axis. ζ is defined as $\underline{\zeta} = \underline{\xi} \times \underline{\eta}$. Because the fluid oscillation forces are generated mainly in the ζ direction and the body axis is in the η direction, we only consider the ξ component of the external torque T_ξ, which can

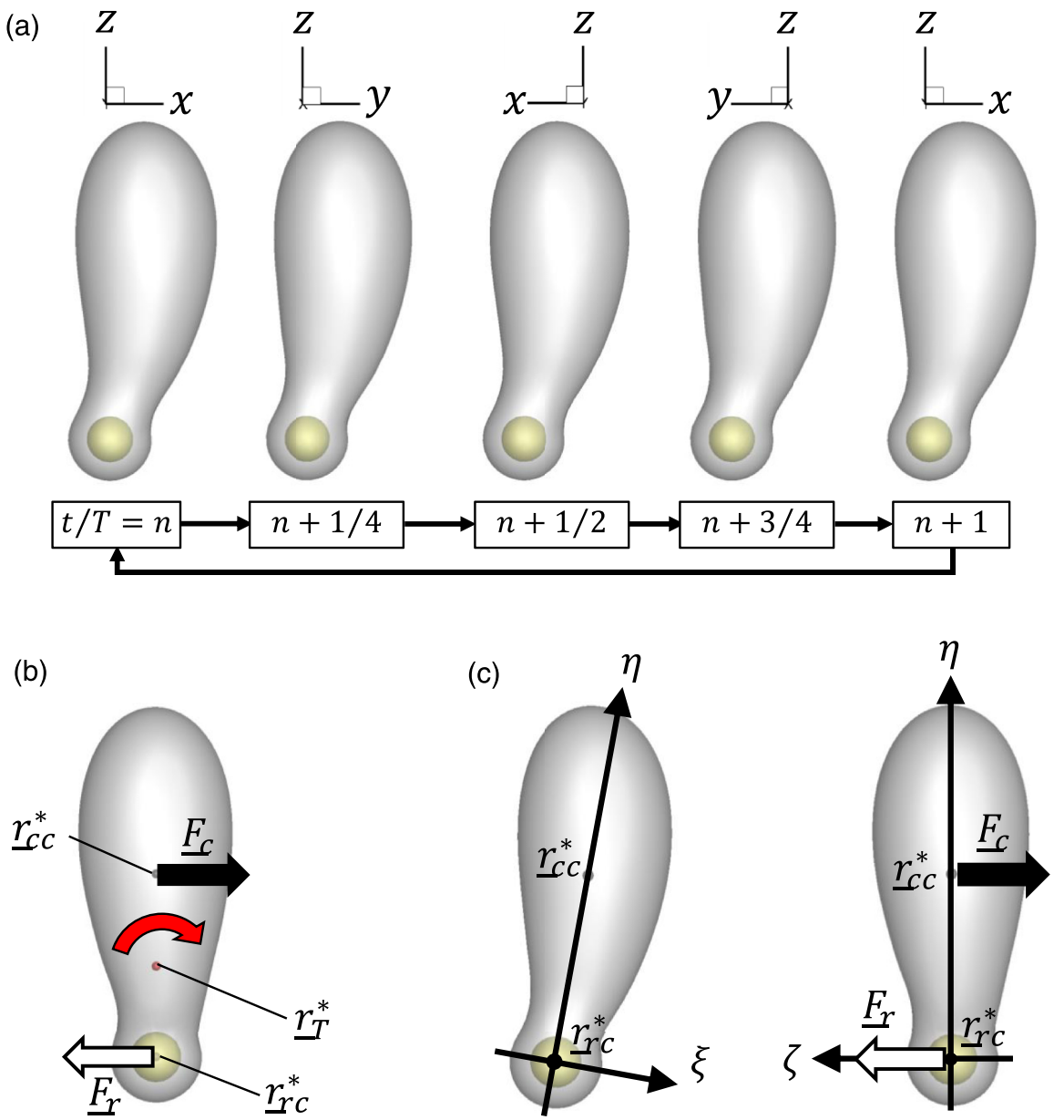

FIG. 6. Propulsion mechanism of the torque swimmer. (a) Shapes of the microswimmer observed in the reference frame rotating with the acceleration field ($a_1/a_2 = 3$, $A_x = A_y = 10$, $\phi_x = 0$, and $\phi_y = -\pi/2$). The coordinate axes of each figure are shown at the top. (b) Schematic diagram of the forces exerted on the rigid sphere $\underline{F_r}$ and the fluid inside the capsule $\underline{F_c}$, as well as the resultant torque that acts at $\underline{r}_T^*$. (c) Another coordinate system $\eta - \zeta - \xi$ with an origin at $\underline{r_{rc}}^*$. The η axis is taken in the direction to $\underline{r_{cc}}$ from $\underline{r_{rc}}$. The ξ axis is defined as $\underline{\xi} = \underline{\eta} \times \frac{(\underline{\eta} \times \underline{z})}{|\underline{\eta} \times \underline{z}|}$, where $\underline{z}$ is the unit vector of the z axis. ζ is defined as $\underline{\zeta} = \underline{\xi} \times \underline{\eta}$.

be expressed as

$$T_\xi = \int (\rho_c - \rho_\infty) g (A r_\zeta - r_z) \underline{n} \times (\underline{r_c} - \underline{r_T}) dS_c + \int (\rho_r - \rho_c) g (A r_\zeta - r_z) \underline{n} \times (\underline{r_r} - \underline{r_T}) dS_r - \int (\rho_c - \rho_\infty) g (A r_\zeta - r_z) \underline{n} \times (\underline{r_r} - \underline{r_T}) dS_r \quad (8)$$

where A ($= A_x = A_y = 10$) is the fluid oscillation amplitude and r_ζ and r_z are ζ and z components of the position vector $\underline{r}$, respectively. The center of torque $\underline{r_T}$ is defined as $\underline{r_T} = (|\underline{F_c}|\underline{r_{cc}} + |\underline{F_r}|\underline{r_{rc}})/(|\underline{F_c}| + |\underline{F_r}|)$. The first term on the right-hand side of Eq. (8) indicates the torque exerted on the capsule by gravity and fluid oscillations. The second term indicates the torque exerted on the rigid sphere by gravity and fluid oscillations. The third term is subtracted to remove duplicated contributions. Equation (8) is solved numerically using the boundary element method to obtain T_ξ.

Once T_ξ is prescribed, we can numerically solve the mobility problem by assuming rigid body motion and force-free conditions. Using the boundary element method, we can obtain the translational velocity $\underline{U}$ and the rotational velocity $\underline{\Omega}$ generated by T_ξ. To take into account the effect of $\underline{\Omega}$

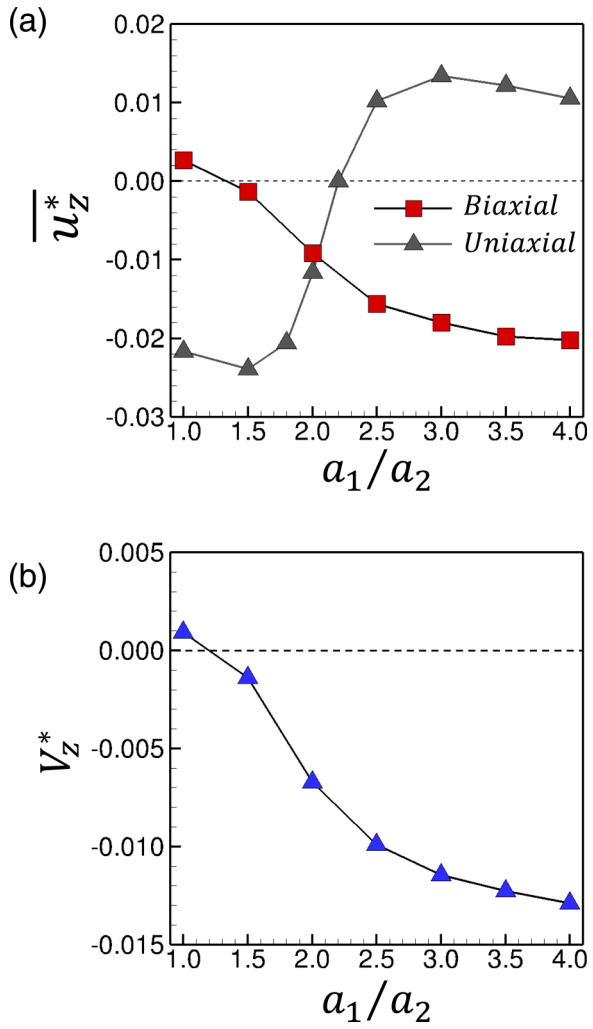

FIG. 7. Effect of the aspect ratio a_1/a_2 on the vertical velocities. (a) The vertical swimming velocity $\overline{u_z^*}$. *Biaxial* indicates the present results under biaxial fluid oscillation conditions. *Uniaxial* indicates the previous results [31] under uniaxial vertical fluid oscillation conditions. (b) The vertical net propulsion velocity V_z^* obtained by assuming rigid body motion.

on the net propulsion, we define the net propulsion velocity $\underline{V}$ as

$$\underline{V} = \underline{U} + \frac{\int \underline{\Omega} \times (\underline{r}_c - \underline{r}_T) dS_c}{\int dS_c}. \tag{9}$$

The z component of the net propulsion velocity V_z of the microswimmer is shown in Fig. 5, with $V_z^* = -0.012$. The actual velocity was about -0.018, close to that obtained from the calculations. Thus, the propulsion mechanism may be explained by the rigid body motion induced by the external torque; a swimmer demonstrating this type of mechanism is referred to as a "torque swimmer."

Consider the three essential ingredients required to generate net propulsion of the torque swimmer: (1) a density mismatch between the rigid sphere and the fluid inside the capsule, (2) gravity, and (3) elasticity of the capsule membrane. As explained in Sec. III B, the density mismatch is necessary to generate external torque. Gravity and capsule membrane elasticity are necessary to induce asymmetric shape deformation for locomotion. Without gravity, the problem setting becomes symmetric with respect to the horizontal plane; thus, in this case, the propulsion direction may become dependent on the initial conditions. Springs are not important in this case, as the rigid sphere remains near the capsule bottom due to external forces.

C. Effect of the aspect ratio

In this section, we show the effect of the aspect ratio, a_1/a_2. We did not vary the other parameters, as in Sec. III C, to emphasize the effect of a_1/a_2, which is considerable.

Figure 7(a) shows the time-averaged vertical propulsion velocity $\overline{u_z^*}$ as a function of a_1/a_2. When $a_1/a_2 = 1$, $\overline{u_z^*}$ was positive and the microswimmer migrated vertically upward. In contrast, when $a_1/a_2 \geqslant 1.5$, $\overline{u_z^*}$ was negative and the microswimmer migrated vertically downward. Thus, the migration direction changes with the aspect ratio.

In Fig. 7(a), $\overline{u_z^*}$ in uniaxial vertical fluid oscillations, obtained from our previous paper [31], is also plotted for comparison. The sign of $\overline{u_z^*}$ reversed itself when a_1/a_2 was larger than 2.4. These results illustrate that the direction of the vertical motion can be altered by changing the fluid oscillation direction, even without changing the other parameters.

We plotted the torque-induced net propulsion velocity V_z^*, introduced in the previous section, in Fig. 7(b). Similar tendencies between V_z^* and $\overline{u_z^*}$ [see Fig. 7(a)] were evident, by which we can confirm that the swimming mechanism can be well explained by the mobility problem of the rigid body with the external torque.

V. CONTROLLING THE MICROSWIMMER TO DRAW A Π-SHAPED TRAJECTORY

In Secs. III and IV, we imposed biaxial fluid oscillations and successfully controlled the microswimmer to migrate both horizontally and vertically. Moreover, by imposing uniaxial vertical fluid oscillations, the direction of migration can be altered [see Fig. 7(a)]. These results illustrate that we are now able to control the microswimmer to migrate in arbitrary directions.

To show controllability, we controlled the microswimmer with $a_1/a_2 = 3$ to draw a Π-shaped trajectory in the x-z plane. The microswimmer was initially placed at the origin of the coordinates. We first imposed uniaxial vertical fluid oscillations with $A_z = 20$ and $\phi_z = -\pi/2$ for $0 \leqslant t^* \leqslant 100$, i.e., for 200 oscillation periods, such that the microswimmer migrated vertically upward. We then imposed biaxial fluid oscillations in the vertical plane with $A_x = 10$, $A_z = 10$, $\phi_x = 0$, and $\phi_z = -\pi/2$ for $100 \leqslant t^* \leqslant 150$, i.e., for 100 oscillation periods, so that the microswimmer migrated horizontally as well as vertically. Last, we imposed biaxial fluid oscillations in the horizontal plane with $A_x = 10$, $A_y = 10$, $\phi_x = 0$, and $\phi_y = -\pi/2$ for $150 \leqslant t^* \leqslant 212$, i.e., for 123 oscillation periods, such that the microswimmer migrated vertically downward. The results are shown in Fig. 8 (see movie 3 in Supplemental Material [39]). We were able to control successfully the microswimmer to draw a Π-shaped trajectory. Thus, the

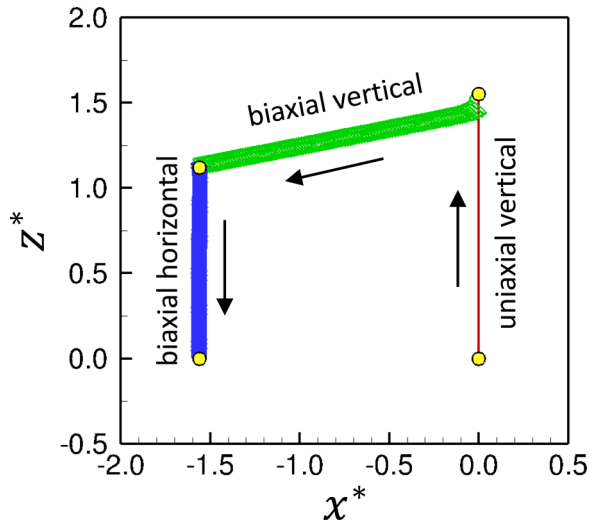

FIG. 8. Controlling the microswimmer with $a_1/a_2 = 3$ to draw a Π-shaped trajectory in the x-z plane (see also movie 3 in Supplemental Material [39]). The microswimmer is initially placed at the origin, and the red line indicates the upward propulsion in uniaxial vertical fluid oscillations with $A_z = 20$ and $\phi_z = -\pi/2$ for $0 \leqslant t^* \leqslant 100$, i.e., for 200 oscillation periods. The green line indicates the horizontal propulsion in biaxial fluid oscillations in the vertical plane with $A_x = 10$, $A_z = 10$, $\phi_x = 0$, and $\phi_z = -\pi/2$ for $100 \leqslant t^* \leqslant 150$, i.e., for 100 oscillation periods. The blue line indicates the results of biaxial fluid oscillations in the horizontal plane with $A_x = 10$, $A_y = 10$, $\phi_x = 0$, and $\phi_y = -\pi/2$ for $150 \leqslant t^* \leqslant 212$, i.e., for 123 oscillation periods.

position and trajectory of the microswimmer can be controlled arbitrarily in three dimensions.

Finally, we compared the efficiency of three kinds of oscillations: (1) uniaxial vertical fluid oscillations, (2) biaxial fluid oscillations in the vertical plane, and (3) biaxial fluid oscillations in the horizontal plane. The efficiency was evaluated by the ratio of the time-averaged propulsion velocity $\overline{U^*}$ to the time-averaged acceleration strength $\overline{|\alpha_g^*|}$, i.e., the migration velocity per unit acceleration strength, as shown in Table I. The time-averaged acceleration strength was calculated as

$$\overline{|\alpha_g^*|} = f^* \int_0^{1/f^*} |\underline{g^*} + \underline{\alpha^*}| dt^*, \tag{10}$$

where $\underline{\alpha}$ is given by Eq. (2). It is found that the biaxial fluid oscillation in the vertical plane is the most efficient among the three kinds of oscillations. It has about four times higher efficiency than the uniaxial vertical oscillations and about two times higher efficiency than the biaxial oscillations in the horizontal plane.

TABLE I. Comparison between the three kinds of fluid oscillations: (a) uniaxial vertical fluid oscillations, (b) biaxial fluid oscillations in the vertical plane, and (c) biaxial fluid oscillations in the horizontal plane. $\overline{U^*}$ is the time-averaged propulsion velocity, and $\overline{|\alpha_g^*|}$ is the time-averaged acceleration strength defined by Eq. (10).

	Uniaxial vertical oscillations	Biaxial oscillations in vertical plane	Biaxial oscillations in horizontal plane
$\overline{u_x^*}$	0.0	3.175×10^{-2}	0.0
$\overline{u_z^*}$	1.344×10^{-2}	2.549×10^{-2}	1.801×10^{-2}
$\overline{u^*}$	1.344×10^{-2}	4.071×10^{-2}	1.801×10^{-2}
$\overline{\lvert\alpha_g^*\rvert}$	12.75	10.05	10.03
$\overline{u^*}/\overline{\lvert\alpha_g^*\rvert}$	1.055×10^{-3}	4.051×10^{-3}	1.797×10^{-3}

VI. CONCLUSIONS

In this paper, we showed that the microcapsule swimmer exhibited rich phenomena by imposing biaxial fluid oscillations. The fluid oscillations induced dramatic change in the propulsion of a microcapsule swimmer, and the propulsion could be controlled in an arbitrary direction. The feasibility in fabricating the microswimmer was not discussed in this paper, as this has already been described and verified in our previous paper [31].

Our present results showed that the microcapsule could be controlled to migrate in the horizontal and vertical directions by imposing biaxial fluid oscillations in the vertical and horizontal planes, respectively. The horizontal propulsion mechanism can be understood in terms of effective and recovery strokes, i.e., as a stroke swimmer, whereas that of vertical propulsion can be represented as torque-induced rigid body motion, i.e., as a torque swimmer. Moreover, by imposing uniaxial vertical fluid oscillations, the direction of migration could be altered. These results illustrate that we are able to control the microswimmer to migrate in arbitrary directions. We demonstrated controllability over the microswimmer by having the microswimmer draw a Π-shaped trajectory in the x-z plane. Thus, both the position and the trajectory of the microswimmer can be controlled arbitrarily in three dimensions. We expect that the results of this paper will be useful regarding future artificial microswimmer designs.

ACKNOWLEDGMENT

This research was supported by Japan Society for the Promotion of Science KAKENHI Grant No. 17H00853.

[1] K. E. Peyer, L. Zhang, and B. J. Nelson, Nanoscale **5**, 1259 (2013).
[2] W. Wang, T.-Y. Chiang, D. Velegol, and T. E. Mallouk, J. Am. Chem. Soc. **135**, 10557 (2013).
[3] R. Dreyfus, J. Baudry, M. L. Roper, M. Fermigier, H. A. Stone, and J. Bibette, Nature (London) **437**, 862 (2005).
[4] P. Tierno, R. Golestanian, I. Pagonabarraga, and F. Sagues, J. Phys. Chem. B **112**, 16525 (2008).
[5] U. K. Cheang, D. Roy, J. H. Lee, and M. J. Kim, Appl. Phys. Lett. **97**, 213704 (2010).
[6] A. Snezhko and I. S. Aranson, Nat. Mater. **10**, 698 (2011).

[7] S. T. Chang, V. N. Paunov, D. N. Petsev, and O. D. Velev, Nat. Mater. **6**, 235 (2007).
[8] G. H. Kwon, J. Y. Park, J. Y. Kim, M. L. Frisk, D. J. Beebe, and S.-H. Lee, Small **4**, 2148 (2008).
[9] G. Loget and A. Kuhn, Nat. Commun. **2**, 535 (2011).
[10] H.-R. Jiang, N. Yoshinaga, and M. Sano, Phys. Rev. Lett. **105**, 268302 (2010).
[11] Z. Fattah, G. Loget, V. Lapeyre, P. Garrigue, C. Warakulwit, J. Limtrakul, L. Bouffier, and A. Kuhn, Electrochimica Acta **56**, 10562 (2011).
[12] S. Thutupalli, R. Seemann, and S. Herminghaus, New J. Phys. **13**, 073021 (2011).
[13] F. Lugli, E. Brini, and F. Zerbetto, J. Phys. Chem. C **116**, 592 (2012).
[14] M. Sentic, G. Loget, D. Manojlovic, A. Kuhn, and N. Sojic, Angew. Chem. Int. Ed. **51**, 11284 (2012).
[15] M. Leoni, J. Kotar, B. Bassetti, P. Cicuta, and M. C. Lagomarsino, Soft Matter **5**, 472 (2009).
[16] J. Li *et al.*, Nano Lett. **16**, 6604 (2016).
[17] J. Elgeti, R. G. Winkler, and G. Gompper, Rep. Prog. Phys. **78**, 056601 (2015).
[18] P. de Buyl and R. Kapral, Nanoscale **5**, 1337 (2013).
[19] R. Golestanian, T. B. Liverpool, and A. Ajdari, New J. Phys. **9**, 126 (2007).
[20] I. Jo, Y. Huang, W. Zimmermann, and E. Kanso, Phys. Rev. E **94**, 063116 (2016).
[21] V. Vladimirov, J. Fluid Mech. **716**, R1-1 (2013).
[22] T. Ishikawa and V. Vladimirov, J. Fluids Eng. **137**, 084501 (2015).
[23] E. M. Purcell, Am. J. Phys. **45**, 3 (1977).
[24] E. Lauga, Soft Matter **7**, 3060 (2011).
[25] A. Shapere and F. Wilczek, Phys. Rev. Lett. **58**, 2051 (1987).
[26] J. E. Avron, O. Gat, and O. Kenneth, Phys. Rev. Lett. **93**, 186001 (2004).
[27] A. Farutin, S. Rafaï, D. K. Dysthe, A. Duperray, P. Peyla, and C. Misbah, Phys. Rev. Lett. **111**, 228102 (2013).
[28] H. Wu *et al.*, Phys. Rev. E **92**, 050701(R) (2015).
[29] H. Wu *et al.*, Soft Matter **12**, 7470 (2016).
[30] B. Nasouri, A. Khot, and G. J. Elfring, Phys. Rev. Fluids **2**, 043101 (2017).
[31] T. Morita, T. Omori, and T. Ishikawa, Phys. Rev. E **98**, 023108 (2018).
[32] T. Omori *et al.*, Phys. Rev. E **86**, 056321 (2012).
[33] D. Matsunaga, Y. Imai, C. Wagner, and T. Ishikawa, J. Fluid Mech. **806**, 102 (2016).
[34] C. Pozrikidis, J. Comp. Phys. **169**, 250 (2001).
[35] R. Skalak, A. Tozeren, R. P. Zarda, and S. Chien, Biophys. J. **13**, 245 (1973).
[36] W. Helfrich, Z. Naturforsch. **28**, 693 (1973).
[37] J. Walter, A.-V. Salsac, D. Barthès-Biesel, and P. L. Tallec, Int. J. Numer. Meth. Eng. **83**, 829 (2010).
[38] T. Ishikawa, M. P. Simmonds, and T. J. Pedley, J. Fluid Mech. **568**, 119 (2006).
[39] See Supplemental Material at http://link.aps.org/supplemental/10.1103/PhysRevE.98.063102 for movies corresponding to figures in text.
[40] C. Brennen and H. Winet, Annu. Rev. Fluid Mech. **9**, 339 (1977).
[41] S. Kim and S. J. Karrila, *Microhydrodynamics: Principles and Selected Applications* (Butterworth, Washington, DC, 1992).